https://doi.org/10.64142/jeai.1.3.35

Journal of Engineering and Artificial Intelligence

ISSN: 3117-3357

Research Article

JEAI-25-35

Python-Scripted Signal Processing Workflow Eliminates Sample-Mount Bias in PXRD of Battery Electrode Materials

Shone A Sarode[*]

Nano Explorers Research Program, University of Texas at Dallas, Richardson, USA

[*]**Corresponding author:** Shone A Sarode, Nano Explorers Research Program, University of Texas at Dallas, Richardson, USA, E-mail: shonesarode183@gmail.com

Received date: October 29, 2025; **Accepted date:** November 05, 2025; **Published date:** November 24, 2025

Citation: Sarode SA (2025) Python-Scripted Signal Processing Workflow Eliminates Sample-Mount Bias in PXRD of Battery Electrode Materials. J Eng Artif Intell Vol.1 No.3: 35.

Abstract

Modern materials research depends on automated measurement systems that can eliminate errors from sample preparation and mounting hardware. This study develops a Python-scripted signal processing workflow that achieves consistent, hardware-independent measurements in Powder X-ray diffraction, an important characterization technique for battery materials, semiconductors and electronic devices. Using a custom GSAS-II automation script, we systematically tested four distinct sample-mounting designs (3D-printed polymer, steel, hybrid polymer-capped steel and commercial zero-background holder) that differ in material composition and geometry, properties known to cause measurement bias in XRD. Eight measurements were collected per mounting design (32 total datasets for TiO_2 reference material; 16 datasets for battery cathode materials NCM 811 and NCM 622). The automated workflow applied the same instrument settings and analysis steps to every dataset, extracting structural parameters, peak positions and signal characteristics without any manual adjustments. Despite the hardware differences between mounts, statistical analysis showed that refined lattice parameters were identical across all mounting types (one-way ANOVA: $p \geq 0.05$ for both a and c), achieving measurement precision of ±0.001 Å approaching research-grade accuracy on a benchtop system. Raw peak position differences between mounts were minimal ($< 0.05^\circ$ in 2θ) and all automated analyses converged with strong signal-to- model agreement ($R_{wp} \leq 15\%$). Testing on NCM battery cathode materials confirmed the same hardware-independent results with small systematic errors. This study establishes an automated, open-source framework that can accelerate XRD-based materials screening for batteries, electronics and sensors. The python-based approach demonstrates how software can correct for hardware differences in measurement systems, advancing the goal of achieving more dependable automated characterization.

Keywords: Automation, Signal processing, Data acquisition, Battery materials, PXRD, XRD, Hardware-independent measurement, Python workflow, Quality control, Sample mounting, Rietveld refinement

Introduction

Powder X-ray diffraction in θ–2θ geometry

Powder X-Ray Diffraction (XRD) probes the ensemble-averaged crystal structure of a polycrystalline specimen by recording the diffracted intensity as a function of the scattering angle 2θ under monochromatic illumination. Randomly oriented crystallites satisfy the Bragg condition at different 2θ, producing a one-dimensional pattern of discrete reflections whose positions, intensities and profiles encode lattice spacings, phase identity and microstructure [1]. A representative diffractometer configuration for laboratory work is the Bragg–Brentano (θ–2θ) para-focusing geometry shown in **Figure 1**, typically with a sealed Cu anode tube (Cu $K\alpha$ radiation) and a scanning detector arm. For an individual Bragg reflection, the condition for constructive interference is given by Bragg's law [2]:

$$n\lambda = 2d\sin\theta. \quad (1)$$

Here n is the diffraction order (usually $n = 1$ in laboratory powder XRD), λ is the X-ray wavelength, d is the lattice-plane spacing and θ is the Bragg angle. Peak positions therefore report interplanar spacings; combined over many reflections, these spacings determine the unit-cell parameters of a crystalline phase. In practice, cell parameters are obtained by whole-pattern least-squares (*e.g.,* Rietveld refinement), which adjusts a structural model to all observed intensities and peak positions simultaneously [3].

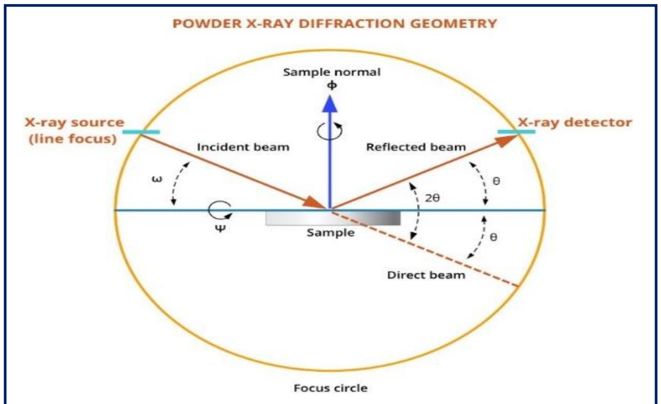

Figure 1: Bragg–Brentano θ–2θ geometry showing X-ray source, sample, detector and focusing-circle configuration. Adapted from MyScope: Training for advanced research, microscopy Australia (CC BY-SA 4.0).

The Bragg–Brentano layout (**Figure 1**) places the source and detector on a focusing circle whose diameter is tangent to the flat specimen surface. As the goniometer scans, the sample rotates by θ while the detector scans 2θ, maintaining the focusing condition [4]. A small specimen height offset Δz (*e.g.,* due to mounting or holder geometry) displaces the sample from the focusing circle and produces a systematic shift of peak positions. To first order, the peak shift for small $\Delta z/R$ is

$$\Delta(2\theta) \approx -\frac{2\Delta z}{R}\cos\theta, \qquad (2)$$

with R the goniometer radius; the magnitude grows with $|\cos\theta|$, so low to mid-angle peaks are most sensitive to Δz. This effect motivates the specimen–holder comparison experiments described in Section II.

Beyond positions, the peak profile carries microstructural information. The Full Width at Half Maximum (FWHM), β, narrows with larger coherently diffracting domain size L and broadens with lattice microstrain ε, after removing instrumental contributions. A commonly used size relation is the Scherrer equation [5]:

$$L = \frac{K\lambda}{\beta\cos\theta}, \qquad (3)$$

where K is a shape factor (≈ 0.9 for spherical crystallites), λ is the wavelength and β is the instrument-corrected FWHM in radians. When both size and strain may contribute, a simple linearization is

$$\beta\cos\theta = \frac{K\lambda}{L} + 4\varepsilon\sin\theta, \qquad (4)$$

the basis of Williamson–Hall analysis. In this study we do not deconvolve size and strain; rather, we use β as a compact, directly measured indicator of peak breadth for specified reflections.

Figure 2 illustrates a typical Cu Kα powder pattern, with a low background, discrete Bragg peaks and a marked FWHM on a representative line. Throughout this paper we evaluate three families of observables: (i) refined lattice parameters (a, c) from whole-pattern fits; (ii) raw peak centers 2θ for diagnostic reflections; and (iii) their FWHM values. These quantities are evaluated across multiple specimen holders to quantify sensitivity to mounting geometry and to establish practical boundaries for routine laboratory measurements.

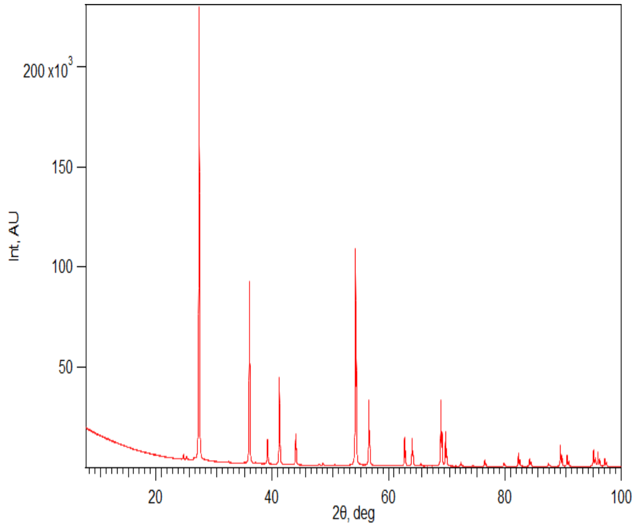

Figure 2: Representative powder XRD pattern of rutile TiO_2 showing intensity versus 2θ. Discrete Bragg peaks exemplify features used for phase identification and lattice-parameter refinement. Adapted from RaidoEnn (Wikimedia Commons, CC BY-SA 4.0).

Bragg's law and diffraction theory

In Bragg–Brentano geometry (**Figure 1**), a monochromatic X-ray beam of wavelength λ impinges on a flat specimen at an incident angle θ while the detector moves at 2θ. Constructive interference occurs when lattice planes with Miller indices (hkl) scatter in phase, producing a diffraction maximum at that scattering angle 2θ. The condition for constructive interference is

$$n\lambda = 2d_{hkl}\sin\theta, \qquad (5)$$

where n is the diffraction order (unity in routine powder work) and d_{hkl} is the interplanar spacing [2]. Equation (5) follows from the path difference construction sketched in **Figure 3**.

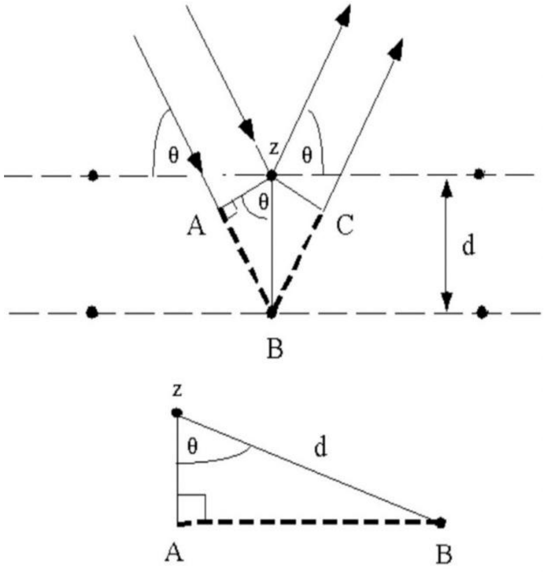

Figure 3: Bragg's law derivation showing interference path difference in reflection geometry. Courtesy of SERC, Carleton College (NSF-funded resource).

This relation defines the one-to-one mapping between peak position and real-space periodicity: Smaller d_{hkl} values correspond to larger 2θ and vice versa. In a powder, all crystallographic orientations are present, so each allowable set of lattice planes contributes a peak; the full pattern (**Figure 2**) thus serves as a fingerprint of both structure (which planes exist and with what spacings) and microstructure (how peaks broaden or skew) [2].

Peak positions determine lattice parameters indirectly. Measured 2θ values are first converted to d*hkl* *via* Bragg's law and then related to the unit-cell metrics (*e.g., a* and *c* for tetragonal or hexagonal symmetries) through the standard metric relations for the crystal system. With several well-resolved reflections, one can estimate *a* and *c* by direct substitution, but modern analyses rely on global least-squares (Rietveld) refinement over the entire pattern. This approach simultaneously optimizes lattice parameters, background, profile coefficients (*U*, *V*, *W*) and small instrumental terms such as zero- shift and specimen displacement [6]. Whole-pattern refinement improves precision, propagates uncertainties correctly and reduces bias from any single reflection.

Because Bragg's law tightly links scattering angles to spacings, small angular systematics can translate into apparent lattice distortions if unmodeled. In flat-plate Bragg-Brentano scans, the dominant effects are (i) specimen displacement - a height offset Δz of the powder surface relative to the diffractometer circle that shifts peaks approximately as $\Delta(2\theta) \propto \cos\theta$; (ii) zero-point offset - a uniform goniometer bias and (iii) transparency or axial-divergence contributions that slightly distort low-angle peak shapes [7]. Proper refinement of displacement and zero terms, together with use of a consistent instrument file, minimizes this systematics so that refined a and c reflect the material rather than the mount [8].

In the work that follows, this framework is applied in two complementary ways. First, for TiO_2 (rutile) powders mounted on four holder types, we test whether the refined *a* and *c* remain statistically indistinguishable when the same scripted GSAS-II refinement is applied, despite holder-dependent raw 2θ offsets and peak-width variations. Second, we evaluate generality on layered cathodes (NCM 811 and NCM 622) by summarizing holder-wise *a*, *c*, key 2θ offsets and FWHM values in a compact table (**Table 1**). Together, these analyses employ Bragg's law as the bridge between angular data and cell metrics, while Rietveld refinement provides the mechanism that separates geometric and instrumental effects from intrinsic structure [3].

Table 1: Battery material validation summary for NCM 811 and NCM 622 layered-cathode compounds. Table shows refined lattice parameters (*a, c*), angular peak offsets (Δ (003)) and peak widths (FWHM (003)) for each mounting configuration (n = 2 measurements per holder). All values reported as mean ± range.

Material	Holder Type	a (Å)	c (Å)	Δ (003) (°2θ)	FWHM (003) (°2θ)
NCM 811	PLA	2.8680 ± 0.0003	14.214 ± 0.003	0	0.27–0.30
	PLA-capped Steel	2.8683 ± 0.0002	14.216 ± 0.002	0.024	0.27–0.30
	Steel	2.8679 ± 0.0003	14.213 ± 0.003	−0.020	0.27–0.30
	ZBH	2.8681 ± 0.0002	14.215 ± 0.002	−0.010	0.27–0.30
NCM 622	PLA	2.8723 ± 0.0003	14.229 ± 0.003	0	0.27–0.31
	PLA-capped Steel	2.8726 ± 0.0002	14.232 ± 0.002	0.024	0.27–0.31
	Steel	2.8722 ± 0.0003	14.229 ± 0.003	−0.020	0.27–0.31
	Zero-Background	2.8724 ± 0.0002	14.230 ± 0.002	−0.010	0.27–0.31

Peak broadening and microstructural interpretation

Building on Section I-B where peak positions (2θ) were linked to lattice spacings through Bragg's law and whole-pattern refinement this section examines the complementary information contained in peak widths and shapes. In powder diffraction, the Full Width at Half Maximum (FWHM) and the overall line profile reflect both instrumental resolution and specimen microstructure; consequently, they serve as quantitative indicators of diffracting-domain size, lattice strain and sample preparation quality [9].

Broadening arises from two main sources. Instrumental broadening is governed by the optics (divergence, spectral dispersion, goniometer resolution) and is typically characterized using standards such as LaB_6 or CeO_2. Sample-induced broadening originates from finite crystallite size, heterogeneous microstrain, stacking faults or preferred orientation. Because the instrumental contribution remains constant under a fixed instrument file, any systematic differences in FWHM among replicate mounts arise from the specimen and mounting process rather than the diffractometer.

Finite crystallite size produces largely angle-independent broadening that can be modeled by the Scherrer relation (Equation 3). In contrast, microstrain contributes angle-dependent broadening that increases toward higher 2θ values [9]. Separation of these effects is commonly achieved through reciprocal- space analysis such as Williamson–Hall plots or through simultaneous profile refinement across many reflections. Modern Rietveld programs (*e.g.,* GSAS-II) represent peak shapes by pseudo-Voigt or double-Voigt functions and refine the profile coefficients (U, V, W, X, Y) alongside lattice constants to account for both size and strain statistically [3,10].

Beyond intrinsic microstructure, specimen geometry and handling can broaden or skew peaks. Variations in packing density, surface flatness or applied pressure during loading may generate residual stress; transparency and axial divergence effects alter low-angle line shapes; and surface-height offsets cause mild asymmetry in Bragg–Brentano scans [11]. Because these factors depend on holder configuration, FWHM functions as a sensitive quality-control metric for comparing mounts under identical optical alignment.

The present study exploits this property: All scans are processed using a shared instrument file and an automated GSAS- II pipeline, ensuring that any observed width variations originate solely from differences in the specimen holder combination. To contextualize these comparisons, Section I-D details the instrument geometry and the four mounts evaluated PLA, PLA-capped steel, steel and zero-background and the procedures used to preserve an invariant instrumental profile across all measurements.

Unit-cell metrics and what we extract from powder XRD

Powder XRD provides two complementary classes of quantitative descriptors that we carry through the paper: unit-cell metrics and profile metrics. The unit-cell metrics are the refined lattice parameters a and c (and by extension the interplanar spacings d_{hkl} derived from them). For tetragonal and hexagonal materials, these two parameters fully specify the average crystal metric and reproducible changes at the 10^{-3} Å level are readily resolvable with laboratory diffractometers when multiple reflections are refined together [12]. The tetragonal unit-cell schematic (**Figure 4**) fixes notation for the case most relevant to this study: Rutile TiO_2, which is tetragonal (space group $P4_2/mnm$) and therefore characterized by one in-plane parameter a and one axial parameter c. Throughout, we report a and c from whole-pattern refinement rather than peak-by-peak estimates to maximize precision and propagate uncertainties consistently across all reflections [3].

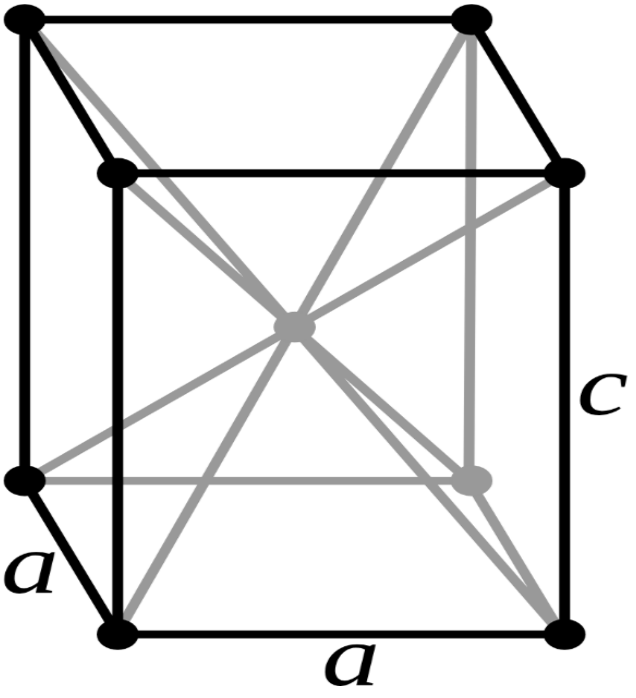

Figure 4: Tetragonal unit cell illustrating lattice parameters a and c (rutile structure, $a \neq c$). Lattice metrics in this work are obtained from powder XRD by whole-pattern (Rietveld) refinement. Adapted from DrBob (Wikimedia Commons, CC BY-SA 3.0).

These lattice metrics are the natural quantities to test for mount-independent reproducibility. Sections I-B–I-C established how Bragg–Brentano geometry maps scattering angles to spacings (Bragg's law) and identified practical sources of small angular systematics (*e.g.*, specimen displacement and zero shift). Rietveld refinement separates those geometric terms from the crystallographic parameters, so that the invariance of refined *a* and *c* across different holders becomes a stringent criterion for data comparability. In the study that follows, we apply exactly the same instrument file, background model and profile function to every scan; holder-wise differences in raw angles or widths are allowed, but if the method is robust the refined *a* and *c* should agree within experimental uncertainty [13].

While *a* and *c* capture the average structure, we also track profile metrics peak centers and Full Widths at Half Maximum (FWHM for a small set of diagnostic reflections. For rutile these serve as internal checks on angular offsets and microstructural line broadening; for layered cathode materials they provide a comparable set of indicators using the (003) and (104) reflections ubiquitous in the battery literature. Together, (i) refined lattice parameters and (ii) a compact panel of peak-level observables form the backbone of the analysis presented in methods (Section II) and results (Section III).

Rietveld refinement and peak-profile modeling

Whole-pattern (Rietveld) refinement provides the quantitative link between the angular data in **Figure 2** and the crystallographic metrics introduced in Sections I-C–I-D. Instead of fitting isolated peaks, the method minimizes the weighted least-squares misfit between observed and calculated intensities over the entire scan:

$$S = \sum_i w_i \left(Y_{\mathrm{obs},i} - Y_{\mathrm{calc},i}\right)^2 , \tag{6}$$

where w_i is typically the inverse variance of $Y_{\mathrm{obs,i}}$ [3]. The calculated pattern depends on scale, background, lattice parameters (*a*, *c*), atomic and thermal parameters, instrument and sample displacement terms and the peak-profile function describing shape and breadth at each 2θ step [9].

Because laboratory PXRD peaks are neither purely Gaussian nor purely Lorentzian, modern implementations adopt a Voigt-type line shape a convolution or mixture of the two (**Figure 5**). In GSAS-II we employ the Thompson–Cox–Hastings pseudo-Voigt (TCHZ) form with a mixing parameter η and a Full Width at Half Maximum (FWHM) governed by the Caglioti relation [3]:

$$\mathrm{FWHM}^2(\theta) = U \tan^2\theta + V \tan\theta + W, \tag{7}$$

augmented by asymmetry coefficients *X* and *Y* to capture low-angle tailing. Within this framework, microstructural broadening is conveniently decomposed into size and strain contributions that, to first order, scale as

$$\beta_{\mathrm{size}} \approx \frac{K\lambda}{L\cos\theta}, \qquad \beta_{\mathrm{strain}} \approx 4\varepsilon\tan\theta, \tag{8}$$

where L is the coherence length and ε the microstrain [9]. Instrumental and geometric effects (*e.g.*, axial divergence, transparency) are absorbed into the profile and asymmetry parameters, while specimen displacement ("sample height") and zero-point offset are refined explicitly to ensure Bragg positions remain consistent with the unit-cell metrics defined in Section I-D [8].

In this study, the scripted GSAS-II pipeline initializes a common instrument file and executes staged refinements scale/background → (*a*, *c*) → profile parameters (*U*, *V*, *W*, *X*, *Y*) → specimen displacement/zero so that correlated variables are introduced in a stable sequence (see Section II). This enables direct, holder-to-holder comparisons of (i) refined lattice constants (Sections III–III), (ii) raw 2θ offsets for diagnostic reflections and (iii) FWHM trends (Section III), while maintaining a consistent physical model across all scans. As reported later, the combination of Bragg's law (Section I-B), the tetragonal metric (Section I-D) and Voigt- based profile modeling (**Figure 5**) decouple small geometric shifts from intrinsic structure in our dataset [14].

Error margins, outliers and statistical interpretation in automated refinement

To close the Introduction, we define the statistical framework used to determine whether holder-dependent differences in diffraction data are meaningful and to ensure that automated Rietveld refinement yields reproducible parameters suitable for cross-mount and cross-material comparison.

Uncertainties and reportable precision: GSAS-II returns standard uncertainties for refined quantities (*e.g.*, lattice constants, zero-point, specimen displacement, profile parameters) from the least-squares covariance matrix [3]. Under the scan conditions and count levels employed, individual peak centers are typically determined to within a few hundredths of a degree in 2θ, which translates after whole-pattern refinement to lattice-parameter uncertainties on the order of 10^{-3} Å. Peak-width (FWHM) uncertainties for well-resolved reflections are on the order of 10^{-2° in 2θ. All figures and tables report per- holder means along with dispersion

https://doi.org/10.64142/jeai.1.3.35
Journal of Engineering and Artificial Intelligence
ISSN: 3117-3357

metrics (standard deviation and interquartile range) so that both central tendency and variability are visible [15].

Outlier detection and treatment: Objective criteria ensure the pipeline remains fully automated yet robust to anomalies. Two complementary rules are applied: (i) $|z| > 3$ screening relative to the global distribution for each quantity and (ii) Tukey's IQR rule, flagging points outside (Q_1 −1.5 IQR, Q_3 + 1.5 IQR) [14]. Flagged points are not removed automatically but are reviewed for physical plausibility using the raw diffraction pattern, refinement log and metadata (*e.g.*, surface flatness, mass loading). If a clear, non-structural cause (mis-leveling, inadequate packing, incorrect scan range) is identified, the scan may be re-measured or excluded with justification; otherwise, it remains in the dataset and is explicitly annotated in the results.

Consistency of modeling across the batch: To prevent modeling parameters from masquerading as holder effects, all refinements use a single instrument parameter file and a common GSAS-II script. The script enforces a fixed scan window (10–60° 2θ for TiO_2; the window for NCM patterns is specified in Section II), the same pseudo-Voigt profile with Caglioti U –V –W broadening, an identical background function and term count and the same set of adjustable geometric terms (zero-point and specimen displacement within bounded ranges). This harmonization ensures that inter-holder variation arises solely from data differences, not model inconsistencies [3].

Pre-specified summary and hypothesis tests: For TiO_2 (rutile), the primary endpoint is equality of refined lattice parameters across holders, assessed *via* one-way ANOVA on per-replicate values of a and c [3]. Secondary, descriptive end-points include holder-wise peak-position offsets for diagnostic reflections and FWHM distributions; these are presented as mean ± SD with IQR shading and compared qualitatively to the global mean in the figures. For the layered oxides (NCM 811, NCM 622), $n = 2$ per holder supports a concise summary (**Table 1**) of holder-wise a, c, $\Delta(2\theta)$ for (003)/(104) relative to PLA and FWHM (003) as mean ± range.

Fit-quality and completeness criteria: Refinements are accepted if they converge and achieve $R_{wp} \leq 15\%$ [14]. All accepted scans are included no curves are manually tuned.

Section II details data acquisition, scripted refinement and statistical computations for **Figures 8** and **Table 1**, while Section III presents these outcomes without interpretation. The Discussion then explores potential physical origins of any remaining holder-dependent differences and the implications for fully automated XRD pipelines.

Materials and Methods

X-ray diffractometer and data collection

All diffraction measurements were performed on a benchtop Rigaku MiniFlex 6G powder diffractometer equipped with a Cu Kα source ($\lambda \approx 1.5406$ Å) operated in Bragg–Brentano parafocusing geometry. The generator was operated at 40 kV and 15 mA using the manufacturer's standard settings for this model class, with factory Bragg–Brentano optics (fixed divergence/receiving slits and axial Soller slits) and a position- sensitive solid-state detector from the Rigaku D/teX family. The instrument's 8-position autosampler enabled unattended batch acquisition; two carriers were used: The OEM metal carousel (**Figure 6b**) and a custom 3D-printed 8-slot tray designed for button-style holders (**Figure 6d**). An overview of the four holder designs evaluated PLA, steel, PLA-capped steel and a commercial Zero-Background Holder (ZBH is shown in **Figure 6a**. CAD schematics of the custom DIP bottom-loading module and the custom 8-slot XRD tray used to standardize preparation and transfer are provided in **Figure 6c**.

Diffraction patterns were collected over 10–80° 2θ. For screening runs and TiO_2 measurements, continuous scans were executed at 10◦ min^{-1} with a step interval of 0.02◦ 2θ; for refinement, the 10–60° region was supplied to the GSAS-II pipeline to exclude very high-angle, low-intensity tails while retaining sufficient Bragg reflections for stable parameter estimation. The sample spinner was engaged (≈15–20 rpm) to improve particle statistics for loose powders and to reduce preferred-orientation effects [16]. All optics and scan settings were held fixed across holder types to isolate the influence of holder geometry and material on the measured patterns.

Instrument calibration and quality control followed established practice for MiniFlex-class diffractometers. Prior to data collection, a line-position standard (NIST SRM 640 Si) was used to verify zero offset and a line-shape standard (NIST SRM 660c LaB6) was used to characterize the instrumental profile function for subsequent refinements [17]. During the campaign, Si standards were measured periodically to check for drift. Measurements were performed at ambient laboratory conditions without a temperature stage. For reproducibility, representative specimens were re-run on different days and autosampler positions; replicate patterns were consistent within the counting statistics of the acquisition.

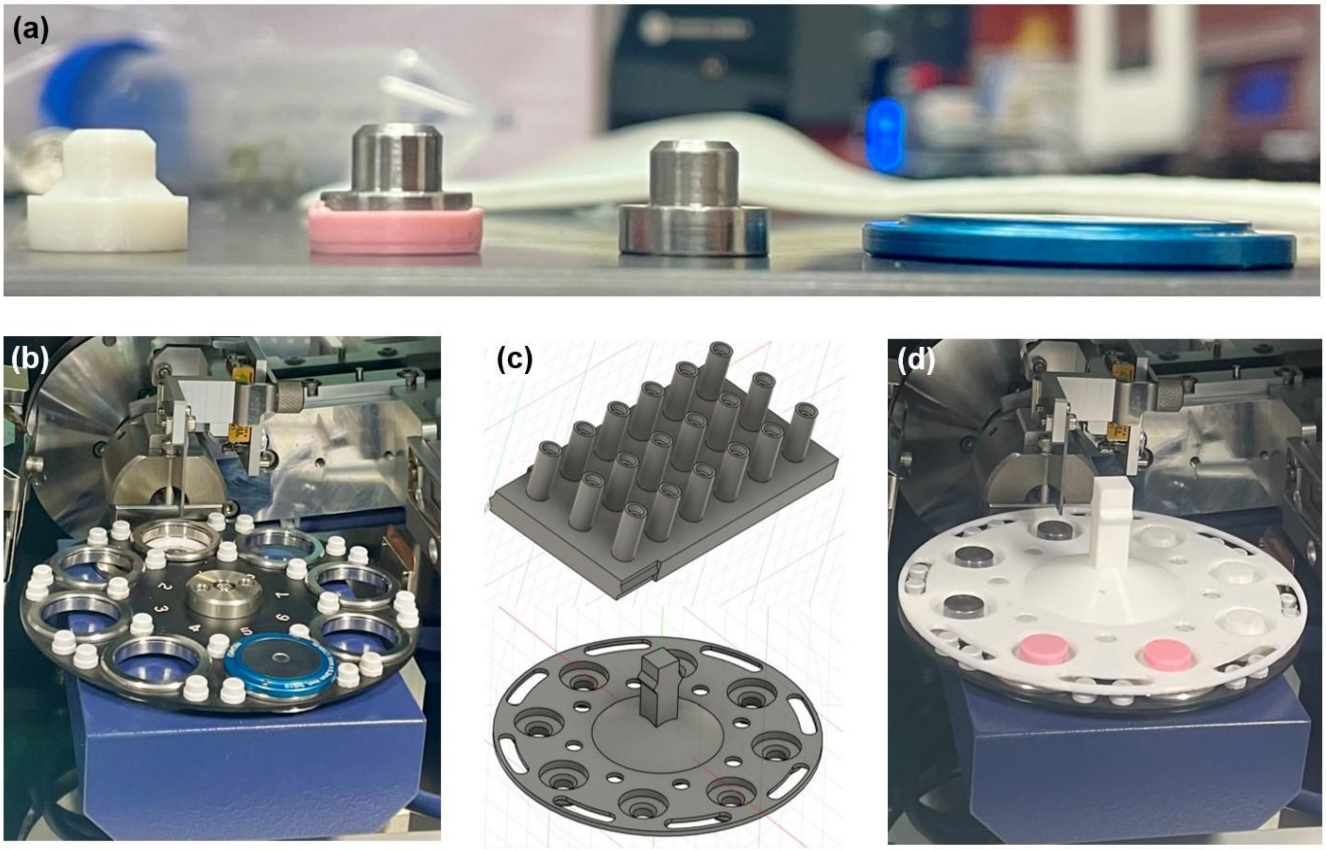

Figure 6: Sample holder hardware and autosampler integration. (a) Side-profile comparison of the four mounts used: PLA, PLA-capped steel, steel and a zero-background holder (ZBH); (b) Rigaku MiniFlex 6G with the OEM 8-position metal carousel; a ZBH occupies one position; (c) CAD renderings of the DIP bottom-loading module (top) and the custom 8-slot 3D-printed carousel (bottom); (d) MiniFlex with the custom 3D-printed carousel carrying button-style holders (PLA, PLA-capped steel, steel).

Raw patterns were exported in Rigaku .ras format and processed by the automated GSAS-II script (Section II-C), which applied a common background model and refined specimen displacement/zero, peak-profile terms and lattice parameters. For runs on the ZBH, transparency-related effects were accommodated by allowing appropriate profile/shape parameters to vary in refinement rather than altering instrument optics, ensuring that instrument conditions remained identical to those used for the button holders [18].

Materials and sample preparation

Titanium dioxide (TiO_2) used for the holder-effects study was produced in a single sol–gel batch, vacuum-dried to a brittle xerogel and lightly hand-ground to a free-flowing powder. From this batch, 32 mounts were prepared 8 per holder type to enable a direct, like-for-like comparison across mounts while avoiding batch-to-batch variability. No pelletizing, binders or adhesive films were used; all measurements were performed on loose powders specifically to isolate holder-induced artifacts.

Four mounts were evaluated: A 3D-printed Polylactic Acid (PLA) button, a PLA-capped steel hybrid, a solid ferritic steel button and a commercial Zero-Background Holder (ZBH). A side-profile comparison of these mounts is shown in **Figure 6a**. Diffraction runs were carried out either with the OEM metal 8-position carousel (**Figure 6b**) or with a custom 3D-printed 8-slot carousel designed to carry button-style holders (**Figure 6d**). For context, CAD renderings of the DIP bottom-loading module and the custom carousel are provided in **Figure 6c**.

Powders were transferred to the button recesses by bottom loading using the custom DIP fixture. In practice, aliquoted powder was first dispensed into individual alumina crucibles (**Figure 7a**). The DIP module an array of vertical posts fitted with the buttons was inverted and gently pressed onto the crucible rack so that each button’s shallow recess contacted the powder pile and filled by contact transfer (**Figure 7b, left**). After loading, buttons were returned upright and placed into the custom 8-slot carousel (**Figure 7b, right**) for insertion into the autosampler. The ZBH was loaded separately by depositing powder directly into its recess and lightly leveling the surface;

no tamping or pressing was applied so that the ZBH data remained comparable to the button mounts.

The powder layer height in each recess was not metered gravimetrically; instead, the surface was leveled visually to be approximately flush with the rim. This deliberate choice mirrors high-throughput practice and introduces small, natural differences in effective *z*-height between mounts precisely the geometric variation that the automated refinement (Section II-C) is intended to correct through displacement/zero and profile terms. To minimize parasitic scattering, stray grains on button flanges were removed with a gentle air puff. All loading was performed by the same operator in a single session using the same motions and contact pressure to reduce operator variability. Button assignments were interleaved across carousel positions so that any position-dependent effects were not confounded with holder type. Immediately after loading, the carousels were transferred to the diffractometer and measured under a single fixed instrument configuration (Section II).

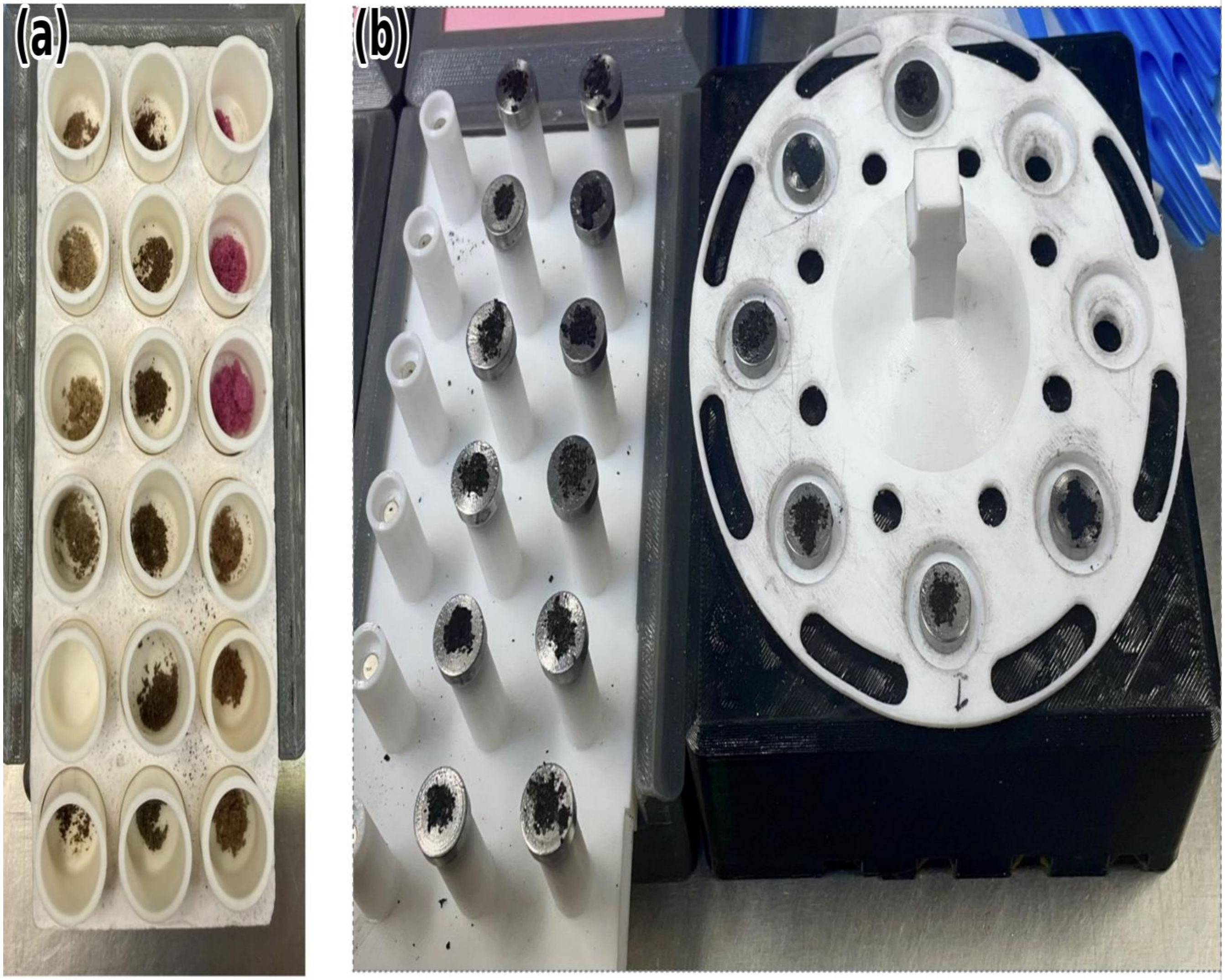

Figure 7: Sample preparation and automated loading hardware. (a) Crucible rack containing aliquoted powder samples prior to XRD measurement; (b) Custom 3D-printed bottom-loading module with steel sample buttons after powder transfer (left) and automated 8-slot carousel with loaded samples positioned for insertion into the Rigaku MiniFlex 6G autosampler (right).

Automated GSAS-II batch refinement and peak-metric extraction

To eliminate operator bias and guarantee identical treatment of every scan, all refinements were executed by a custom Python pipeline driving the GSAS-II scripting API. For each Rigaku .ras file the script instantiated a fresh GSAS-II project, attached a common instrument parameter file (instrument_refined.instprm) and enforced a fixed refinement sequence. The TiO_2 batch comprised 32 mounts (8 per holder: PLA, PLA-capped steel, steel, ZBH); the identical pipeline was also applied to small validation sets of NCM 811 and NCM 622 (2 mounts per holder each), while the primary analysis and statistics center on TiO_2.

Histogram limits and background modeling: All histograms were evaluated over 10–60° 2θ, which retains the dominant reflections needed for stable lattice and profile refinement while avoiding very high-angle regions with poor counting statistics. A two-component background model was applied uniformly: (i) an automatic smooth background with four refined coefficients and (ii) a broad pseudo-peak centered near $\sim 15^\circ\ 2\theta$ to absorb slowly varying diffuse intensity. After these terms converged, fixed-point fitting was invoked to stabilize the baseline before structural parameters were enabled.

Staged refinement strategy: To manage parameter correlations, refinement proceeded in blocks. Following an initial scale/background pass, specimen-level terms were enabled to correct mounting differences: Sample shift/displacement (including in-plane DisplaceX/DisplaceY) and absorption/contrast to accommodate small variations in packing or holder material. Instrumental parameters were then refined in a defined order: Axial asymmetry (SH/L) and the 2θ zero first, followed by progressive activation of Gaussian Caglioti coefficients W, then (V, W) and finally (U, V, W). This ordering ensures that geometric misalignment is captured by displacement/zero rather than by artificially broadening peaks. Cycle limits (up to 100 per block) and deterministic save points were scripted to yield reproducible convergence across the batch.

Phase model and microstructure: The phase model explicitly separated sample and holder contributions. For TiO_2, rutile (bounds a, $b \approx 4.4$–4.8 Å, $c \approx 2.8$–3.1 Å) and anatase (a, $b \approx 3.6$–3.9 Å, $c \approx 9.3$–9.5 Å) were included; an elemental Fe phase (bcc, $a \approx 2.8$–3.0 Å) accounted for steel-derived diffraction, preventing spurious assignment of holder intensity to the sample. For each histogram–phase (HAP) pair the same sequence was used: Scale → Cell → Size (iso.) → HStrain (iso.) → Mustrain (generalized). After a block converged, its terms were frozen before the next block was enabled. Atomic positional/thermal parameters were left fixed (or minimally adjusted) once microstructural terms stabilized, as the study focuses on lattice-level metrics rather than detailed atomics.

Quality control and traceability: For every refinement the script recorded the weighted profile R-factor (R_{wp}), saved the residual trace and generated a diagnostic plot overlaying observed, calculated and difference curves within the 10–60° window. Reflection markers were computed from the refined unit cells (Cu $K_{\alpha 1}$ wavelength from the instrument file) and rendered as vertical ticks to visually confirm indexing. All figures were saved as PNGs with the button identifier in the filename and a timestamped log captured each action and any exception.

Peak metrics: Because holder effects are most directly expressed in peak position and width, the pipeline extracted these metrics in a standardized manner after refinement. The observed intensity array was lightly smoothed (Savitzky–Golay) and a first-derivative zero-crossing test located local maxima. Within small windows around three diagnostic reflections 25.3°, 44.7° and 48.5° 2θ (strong TiO_2 and Fe peaks the routine selected the highest local maximum and recorded its centroid. Full Width at Half Maximum (FWHM) was computed directly from the observed profile by linear interpolation at half-maximum on each side of the apex, avoiding model-dependent width assumptions. Per-button metrics (peak position and FWHM for each target reflection) were written row-wise to a CSV ledger.

Phase fractions (consistency check): For completeness the script reported internally consistent phase fractions by normalizing the products of refined scale factors and formula masses across phases in each histogram. Absolute quantification was not the goal; these fractions help verify that Fe- derived intensity is correctly attributed to the holder rather than to the TiO_2.

Outcome: End-to-end project creation, histogram im- port, background modeling, staged specimen/instrument and phase refinement, microstructure and metric extraction ran without manual intervention once launched. Identical instrument and refinement settings were enforced for every dataset. The pipeline converts raw .ras scans into the specific quantities interrogated in the results: (i) refined lattice parameters as the primary structural-fidelity metric; (ii) raw peak positions as a direct indicator of holder-induced z-height differences and (iii) FWHM values as diagnostics for preparation or holder induced broadening. Source code is archived as listing S1.

Experimental procedure

TiO_2 was used as the primary validation cohort. All TiO_2 powder originated from a single sol–gel batch and was subdivided into independent aliquots for mounting. Four holder designs were evaluated: Fully 3D-printed PLA, ferritic steel, PLA-capped steel and a commercial Zero-Background Holder (ZBH). For each holder type, eight independent TiO_2 aliquots were measured (n = 8 per holder; 32 scans total). Powders were bottom-loaded using the laboratory DIP pipeline: The recessed face of each button was gently pressed into the post-calcination powder bed contained in alumina crucibles, allowing the cavity to fill without tamping or binders. Loose grains on the button flange were removed with a gentle air puff to yield a nominally planar surface. Buttons were then placed into a custom 8-position tray compatible with the benchtop autosampler and transferred to the diffractometer. No cover films were used.

Data acquisition was performed on a Rigaku MiniFlex 6G in Bragg–Brentano geometry with Cu Kα radiation, operated at 40 kV and 15 mA under a single, fixed optics configuration (Section II). The sample spinner was engaged (≈15–20 rpm) for all measurements to improve particle statistics in loose powders while holding all other settings constant across holder types. Scans were collected over 10–80° 2θ with a nominal step of 0.02° at ~ 10° min^{-1}. A recent pro- file/zero calibration was embedded in the instrument parameter file (instrument_refined.instprm) and applied uniformly. To minimize confounding by time or position, the run order was interleaved across holder types and autosampler positions were rotated; ambient laboratory conditions were constant over each batch. No deliberate misalignment was introduced the study leverages natural geometric differences between holders.

Immediately after acquisition, each raw pattern (.ras) entered the same automated GSAS-II pipeline described in Section II-C. For all scans, the refinement window was restricted to 10–60° 2θ; backgrounds were modeled by an automatic smooth function plus a broad low-angle term; and geometry/profile terms (specimen displacement/zero and U–V–W) were refined before phase-specific parameters. TiO_2 refinements included rutile as the primary phase, with anatase permitted when warranted by the pattern; a bcc-Fe phase was included whenever steel or PLA-capped steel buttons were present to capture holder diffraction. For each scan, the script exported refined lattice parameters (a, c), centroided positions of predefined diagnostic reflections, corresponding FWHM values computed directly from the observed intensity profile, the weighted profile R-factor (R_{wp}) and a plot of observed/calculated/residual intensities with phase ticks. No scans were excluded *a* priori. Refinements with $R_{wp} > 15\%$ were flagged for review; in the TiO_2 cohort, all runs satisfied the acceptance criterion.

Two layered cathode compositions (NCM 811 and NCM 622) were measured as a compact generalization set using the identical mounting, acquisition and refinement pipeline. For each composition, two aliquots per holder were collected (n = 2 per holder; 16 scans total across both NCMs). Given the limited n, these data are treated in Section III as corroborative trends rather than subjected to the full inferential framework applied to TiO_2.

Data analysis and evaluation criteria

The primary endpoint was invariance of refined lattice parameters with respect to holder type for TiO_2. For each holder, the mean and standard deviation of a and c were computed across $n = 8$ replicates. A one-way analysis of variance (ANOVA, $\alpha = 0.05$) tested for a holder effect on each parameter; when variances were unequal by Levene's test, Welch's ANOVA was used. If ANOVA returned $p \geq 0.05$, holder equivalence was concluded; if $p < 0.05$, pairwise post hoc comparisons (Tukey HSD or Games–Howell for unequal variances) localized the differences. In addition to hypothesis testing, 95% confidence intervals and coefficients of variation were reported to convey practical significance. A priori, lattice-parameter consistency was defined as (i) no holder effect by ANOVA and (ii) an across-holder standard deviation on the order of 10^{-3} Å, consistent with high-quality benchtop PXRD.

Secondary endpoints: Raw peak positions (2θ) were extracted directly from the observed intensity for diagnostic reflections: TiO_2 peaks at ~ 25.3° and ~ 48.5° and when steel or PLA-capped steel were used the Fe (110) reflection at ~ 44.7° as a holder marker. Because refinement adjusts model parameters but not the measured maxima, systematic shifts in 2θ were interpreted as specimen-height (z-displacement) differences between holders, rather than structural change.

Peak broadening analysis: Full Width at Half Maximum (FWHM) for the same reflections was computed directly from the observed profiles *via* half-maximum interpolation. Between-holder differences in FWHM were interpreted as arising from packing, surface planarity, transparency–absorption mismatch or loading-induced microstrain rather than structural inaccuracy. For these endpoints, descriptive statistics and distributional plots (*e.g.*, scatter plots with per-holder mean bands or box/violin plots) were emphasized; variance-equality tests were reported as supporting evidence, with no strict pass/fail threshold on FWHM.

Quality control: For each refinement, R_{wp} and the residual trace were recorded; refinements with $R_{wp} \leq 15\%$ were retained for analysis. Outliers in any metric were defined as $|z| > 3\sigma$ relative to the TiO_2 cohort and were retained but flagged for discussion when preparation cues (*e.g.*, irregular surfaces) were present. All plots and statistics were derived from the script-exported CSV to preserve provenance. The NCM 811 and NCM 622 datasets (two aliquots per holder per composition, n = 2) were processed identically; given the limited n, these data are reported as mean ± range to corroborate the TiO_2 conclusions without repeating full inferential testing.

Results

Lattice parameters (TiO_2)

Refined rutile lattice parameters were statistically indistinguishable across holders (**Figures 8a, 8b**). A one-way ANOVA detected no holder effect for either parameter (a: $p \geq 0.05$; c: $p \geq 0.05$). Across the 32 TiO_2 scans, the global means were a = 4.5930 Å (σ = 0.0011 Å) and c = 2.9594 Å (σ = 0.0014 Å). Per-holder means were narrowly centered about the global means; the separation between any two-holder means was $\lesssim$ 0.002 Å and the interquartile bands for the four holders overlapped strongly in both a and c. Replicate scatter within each holder was small and comparable across mounts.

Peak positions in 2θ (TiO_2)

Raw peak centers for two diagnostic reflections exhibited small, repeatable offsets among holders (**Figures 8c, 8d**). For Peak 1, the global mean was 25.352° ± 0.022° (mean ± SD); holder centroids spanned ~ 0.06° and within-holder spreads were tightly clustered around the per-holder means. For Peak 2, the global mean was 48.483° ± 0.022°; holder centroids differed by ~ 0.05°. In both cases, the four interquartile bands overlapped but were slightly shifted in 2θ relative to one another, while replicate variance within each holder remained modest and of similar magnitude.

Peak widths (TiO_2)

FWHM values were tightly distributed around the global means with substantial overlap among holders (**Figurers 8e and 8f**). For Peak 1 (≈ 25°), the global mean was 0.277° 2θ with $\sigma \approx 0.021°$; per-holder means lay within ~ 0.02° of one another and within-holder interquartile widths were ~ 0.015–0.025° 2θ. For Peak 2 (≈ 48°), the global mean was 0.552° 2θ with $\sigma \approx 0.111°$; per-holder means clustered in the ~ 0.52–0.58° 2θ range and the interquartile widths were broader than for Peak 1 yet still overlapped across holders.

Ordering by holder (**Figurers 8e and 8f**) suggests steel tending to the lowest FWHM, ZBH slightly higher and PLA/PLA- capped intermediate, though the distributions remain largely overlapping.

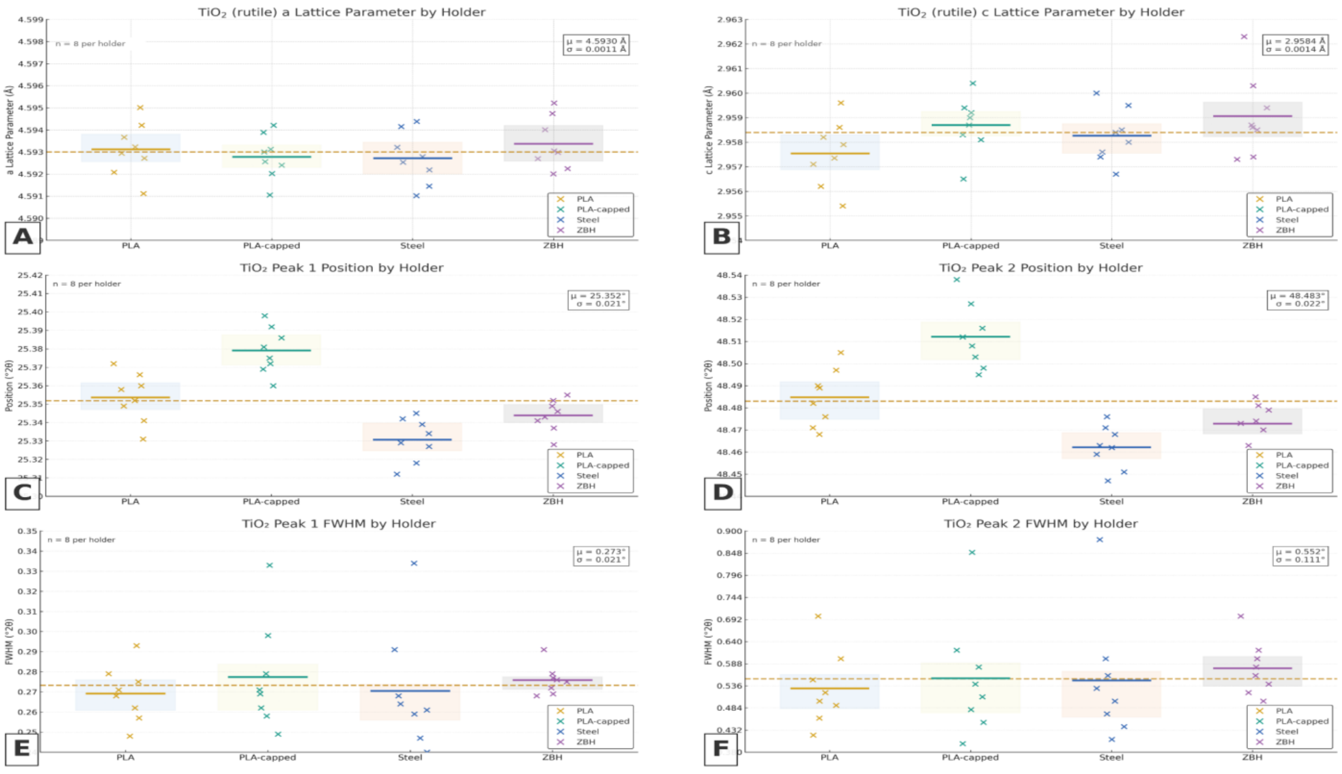

Figure 8: Statistical validation of XRD measurements for TiO_2 reference material. (A,B) Refined rutile lattice parameters (a, c) are statistically equivalent across all holders ($p \geq 0.05$, ANOVA; n = 8 per holder); (C,D) Raw peak positions (2θ) for diagnostic reflections show holder-dependent offsets < 0.10°; (E,F) FWHM from observed profiles demonstrate consistent signal quality. Boxes indicate interquartile ranges; crosses show individual replicates; dashed lines mark global means and solid lines mark per holder means.

Layered cathode checks (NCM 811, NCM 622)

For NCM 811, holder-averaged lattice parameters were a = 2.8679–2.8683 Å and c = 14.213–14.216 Å; Δ (003) offsets relative to PLA were +0.024° (PLA-capped), −0.020° (steel) and −0.010° (ZBH). Similarly computed Δ (104) offsets (not shown) were +0.030°, −0.030° and −0.010°, respectively. FWHM (003) values were 0.27–0.30° 2θ (mean ± range, n = 2 per holder).

For NCM 622, holder-averaged lattice parameters were a = 2.8722–2.8726 Å and c = 14.229–14.232 Å; Δ (003) offsets relative to PLA were +0.024° (PLA-capped), −0.020° (steel) and −0.010° (ZBH). Similarly, Δ (104) offsets (not shown) were +0.030°, −0.020° and −0.010°, respectively. FWHM (003) values were 0.27–0.31° 2θ (mean ± range, n = 2 per holder). Given the limited n, these data are presented as corroborative trends rather than subjected to the full inferential framework applied to TiO_2 (**Table 1**).

Fit statistics and completeness

All scripted refinements converged under the predefined acceptance criterion ($R_{wp} \leq 15\%$); no scans were excluded. The exported CSV file and per-scan diagnostic plots document the observed, calculated and difference profiles together with phase tick marks for traceability (see Section II-C); inclusion of fit indicators (*e.g.*, R_{wp}) and per-pattern diagnostics is standard in Rietveld reporting [19].

Discussion

Specimen displacement and holder-dependent 2θ shifts

In a Bragg–Brentano para-focusing diffractometer, a vertical offset of the diffracting surface from the goniometer circle introduces a systematic shift in peak positions that scales approximately with the tangent of the Bragg angle; this “specimen displacement” term is a well-established geometric artifact distinct from any change in lattice spacing [20]. Under the bottom-loading protocol used here, loose powders were loaded without tamping or binders and the surface was leveled by gentle contact with the recess rim. Small differences in effective surface height are therefore expected across mounts with different recess geometries and materials, even when the operator follows a standardized motion sequence [8].

The holder-dependent offsets observed in **Figure 8c and 8d** are consistent with this mechanism: Peaks recorded on different mounts exhibit repeatable, mount-specific shifts on the order of a few hundredths of a degree, while within-mount scatter remains modest. In Rietveld modeling, such angular misalignments are represented by specimen displacement and zero-point correction parameters, allowing geometric and instrumental offsets to be absorbed by those terms rather than erroneously incorporated into refined lattice constants [6].

Because lattice parameters are constrained by the simultaneous fit to many reflections across 2θ, refinement can preserve the metric invariance of the unit cell even when raw peak centers differ by mount. The scripted GSAS-II pipeline used here explicitly enabled displacement/zero terms prior to peak-profile refinement, which is the recommended sequence for maintaining identifiability of lattice parameters in the presence of geometric systematics [10].

Peak widths (FWHM): Preparation and optical contributions

Small differences in FWHM among mounts (**Figures 8e,8f**) are readily rationalized by preparation and optical effects that broaden peaks without altering average lattice metrics. In Bragg–Brentano geometry, axial divergence and footprint truncation contribute to an angle-dependent broadening envelope that is instrument and optics-specific [21]. On top of that envelope, holder material and surface condition modulate the apparent width.

Zero-background plates (*e.g.*, polished single-crystal substrates) can exhibit partial transparency and specimen-thickness effects that broaden peaks symmetrically at higher angles, whereas metallic mounts with higher absorption reduce effective penetration and can yield slightly narrower profiles for otherwise identical powders [5]. For loose powders prepared by gentle bottom-loading, residual height undulations and small differences in packing density produce additional, preparation-limited broadening; preferred orientation is usually reduced relative to tamped pellets but not eliminated, especially for platy or acicular grains [4].

The pattern in **Figures 8e, 8f** substantial overlap of holder-wise FWHM distributions, with per-holder means ordered from slightly narrower (steel) to slightly broader (ZBH) and intermediate values for PLA-based mounts accords with these non-structural influences. Within a whole-pattern fit, pseudo-Voigt (or double-Voigt) profile functions partition Lorentzian like size terms from Gaussian-like strain/axial terms, permitting modest FWHM differences to be captured by profile coefficients without forcing changes to the refined unit cell. The absence of a corresponding trend in refined a and c (**Figures 8a, 8b**) is therefore expected when geometric and microstructural broadening are modeled explicitly [10].

Refinement strategy and parameter identifiability

Parameter identifiability in Rietveld analysis depends on model completeness and the order in which correlated terms are introduced [14]. The scripted GSAS-II sequence adopted here prioritized geometric corrections specimen displacement and zero-point before any modification of peak-profile coefficients, ensuring that global angular systematics were corrected without allowing width parameters to compensate for geometric misalignment. Gaussian U–V–W terms (Caglioti law) were then introduced progressively, followed by isotropic crystallite-size and microstrain terms; this staging reduces covariance between lattice constants and profile parameters, particularly in limited angular windows. A complete phase model was maintained throughout, including a bcc-Fe holder phase when steel or PLA-capped mounts were used, so that any mount-derived diffraction could be attributed correctly and not spuriously absorbed into the sample phase(s) [8].

This refinement strategy explains the integrated pattern observed in **Figure 8**: Lattice parameters remain invariant across mounts (panels (a)–(b)) despite mount-specific 2θ shifts (panels (c)–(d)), while modest differences in FWHM are captured by profile/microstructural terms (panels (e)–(f)) rather than propagating into the unit-cell metrics. By enforcing a fixed, literature-consistent refinement order and phase set in an automated script, the pipeline preserves structural fidelity while retaining diagnostic sensitivity to geometric and preparation variables precisely the separation of information streams required for reliable, high-throughput PXRD pipelines [22].

Generalization beyond TiO_2

To assess whether holder-dependent effects and the scripted refinement pipeline extend beyond simple oxides, layered NCM cathodes provide a stringent validation case: They differ from TiO_2 in elemental absorption (Ni, Co, Mn *vs.* Ti), often display basal-plane texture and can exhibit anisotropic microstructure relative to equiaxed rutile grains [23]. Two compositions NCM 811 and NCM 622 were mounted, measured and refined with the identical pipeline used for TiO_2.

Across holders, the holder-averaged lattice parameters of NCM 811 and NCM 622 agreed within $\leq 10^{-3}$ Å when processed with the same instrument file and refinement sequence. For two diagnostic reflections, the between-holder 2θ spans were on the order of a few hundredths of a degree and FWHM values were of similar magnitude across holders; per- holder means and ranges are summarized in **Table 1**. Given the limited sample size ($n = 2$ per holder per composition), these results are presented as corroborative trends rather than as a powered equivalence test. The observed patterns are consistent with the TiO_2 results and support the geometric interpretation of holder effects established in the preceding subsections.

Implications for automated PXRD

The scripted pipeline developed here enables practical decoupling of structural, geometric and microstructural information in unattended, high-throughput PXRD. Three features are essential to that outcome: First, a fixed refinement order that prioritizes specimen displacement/zero before profile terms and then introduces size/strain in a controlled sequence; second, per-scan export of the specific metrics used for downstream checks (lattice parameters as structural outputs; measured 2θ centers as geometric indicators; FWHM as a preparation/line-profile descriptor); and third, uniform instrument parameters across all measurements.

Together, these elements yield quantitative acceptance gates that can be applied consistently within a given instrument configuration: Invariance of a and c across holders at 10^{-3} Å, bounded 2θ spans for designated reflections (*e.g.*, $\leq 0.10^{\circ}$ across holders) and FWHM values that remain within interquartile bands established on reference powders. These thresholds are instrument and optics-specific but are stable for a fixed configuration, enabling consistent quality control across campaigns. In contrast, manual, ad hoc refinement pipelines where operators iteratively adjust parameters by visual fit quality can inadvertently compensate geometric artifacts (*e.g.*, specimen displacement) by tuning structural or microstructural terms, increasing operator-dependent variability [14]. A scripted approach enforces parameter sequencing, records decisions and produces auditable outputs (plots and CSVs) suitable for automated pipelines.

Limitations and threats to validity

Scope and sampling: The TiO_2 cohort ($n = 8$ per holder) supports inference at the holder level within one instrument/optics configuration. The NCM cohort ($n = 2$ per holder per composition) is confirmatory rather than inferential; its agreement is reported as a consistency check rather than a powered test of equivalence. All data were acquired on a single benchtop Bragg–Brentano diffractometer under fixed optics. Absolute magnitudes of 2θ spans and FWHM differences will depend on source, optics and detector details and may differ on other platforms.

Preparation and modeling choices: Preparation was deliberately constrained to lose powders loaded by the same bottom-loading protocol without binders or cap films. Alternative preparation modes (tamped pellets, adhesive films, spinner use) could shift the balance between geometric and microstructural broadening channels. Phase models included a bcc-Fe holder phase when steel-containing mounts were present; however, weak mount-derived features below the fit threshold could influence local backgrounds. Preferred orientation and anisotropic strain were treated with isotropic terms to preserve comparability; strongly textured powders may require anisotropic models. The refinement window (10–60° in 2θ) stabilized fits and matched counting statistics but excludes very high-angle reflections; different windows can alter parameter covariance.

Acceptance criteria and external validity: Acceptance criteria (*e.g.*, $R_{wp} \leq 15\%$) and outlier handling (retain all scans; flag $|z| > 3\sigma$) were pre-specified to balance rigor with throughput. Tighter gates or more aggressive curation could further reduce variance at the cost of manual review. Numerical thresholds derived here (*e.g.*, $|\Delta a|$, $|\Delta c| \leq 10^{-3}$ Å; 2θ span ≤ 0.10°) should not be transplanted directly to other instruments, materials or preparation modes without local validation.

Synthesis: These limitations reflect deliberate design choices for an initial validation study: A single instrument with fixed optics isolates holder effects from instrumental variability; loose powders mirror common high-throughput practice; TiO_2 offers a robust, well-characterized benchmark, whereas NCM materials probe a distinct structural class; and isotropic models prioritize stability for exploratory comparisons. Within this scope, the internally consistent patterns provide a validated foundation for broader extensions outlined below.

Practical recommendations and future work

Immediate recommendations for practice: For day-to-day operation in high-throughput labs, standardize bottom-loading with a rigid jig and consistent recess geometry; randomize autosampler slots by holder type to decouple carousel position from mount; maintain a fixed refinement order (displacement/zero $\rightarrow U - V - W \rightarrow$ size/strain) under a version-controlled instrument file; include a holder phase (*e.g.*, bcc-Fe) whenever steel-containing mounts are used; apply quantitative QC gates ($|\Delta a|$, $|\Delta c| \leq 10^{-3}$ Å across holders; designated-peak 2θ spans ≤ 0.10°; FWHM within established interquartile bands); and archive per-scan plots/CSVs for traceability.

Among these, enforcing a fixed refinement order and complete phase models are critical for structural accuracy; QC gates and standardized loading improve precision, while randomization and archiving bolster reproducibility and troubleshooting.

Future validation studies: Three extensions would most strengthen generalizability. First, expand the materials set to additional chemistries and microstructures (*e.g.*, layered oxides with stronger texture, spinels, bronzes) with sufficient n per holder to enable powered across-holder tests. Second, evaluate robustness across instruments and optics (parallel-beam geometries, alternative axial optics, different detectors) to quantify platform dependence of geometric and width signatures.

Third, incorporate internal-standard mixtures (*e.g.*, admixed Si or LaB_6) to enable absolute lattice-parameter calibration independent of specimen displacement, supporting cross-campaign and inter-laboratory traceability at the 10^{-4} Å level [20]. These extensions would both strengthen the robustness of the scripted pipeline and enable its deployment in autonomous materials-discovery pipelines, where structural decisions must be made reliably from samples prepared across diverse holder configurations and loading conditions.

Conclusion

The automated GSAS-II refinement pipeline effectively eliminates sample-mount–induced biases and delivers consistent lattice parameters across diverse holder designs. These results confirm that automated, software-driven analysis can provide reproducible and hardware-independent PXRD measurements suitable for high-throughput materials research.

Code Availability

The Python automation scripts used in this study are available as open-source software at https://gist.github.com/shonesarode/3c974b365d956f8d52e58acbc32227ca. Includes GSAS-II refinement automation routines, data extraction and statistical analysis code.

Acknowledgments

I thank my research mentor M.B. for his steady guidance and clear feedback. I am grateful to the Multiscale Simulation Lab at the University of Texas at Dallas for access to equipment and for day-to-day support from labmates.

This project was completed as part of the NanoExplorers program. Thanks also to my teachers and family for their encouragement. Any mistakes are my own.

References

1. Dinnebier RE, Scardi P (2021) X-ray powder diffraction in education. Part I. Bragg peak profiles. J Appl Crystallogr 54: 1811-1831. [Crossref], [Google Scholar], [Indexed]
2. Pope CG (1997) X-ray diffraction and the bragg equation. J Chem Educ 74 129-129. [Crossref], [Google Scholar]
3. McCusker LB, Von Dreele RB, Cox DE, Loue¨r D, Scardi P (1999) Rietveld refinement guidelines. J Appl Crystallogr 32 36-50. [Crossref], [Google Scholar]
4. Ahtee M, Nurmela M, Suortti P, Järvinen M (1989) Correction for preferred orientation in rietveld refinement. J Appl Cryst 22: 261-268. [Crossref], [Google Scholar]
5. Noyan MA, Noyan IC (2024) Sampling volumes in powder diffraction experiments. Powder Diffr 1-13. [Crossref], [Google Scholar]
6. Tsubota M, Kitagawa J (2017) A necessary criterion for obtaining accurate lattice parameters by rietveld method. Sci Rep 7: 15381. [Crossref], [Google Scholar], [Indexed]
7. Hwang BH (1996) Shifts of peak positions due to specimen geometry and beam divergence in X-ray diffractometer. Powder Diffr 11: 276-280. [Crossref], [Google Scholar]
8. Hulbert BS, Kriven WM (2022) Specimen-displacement correction for powder X-ray diffraction in Debye-Scherrer geometry with a flat area detector. J Appl Crystallogr 56: 160-166. [Crossref], [Google Scholar], [Indexed]
9. Scardi P, Ermrich M, Fitch AN, Huang EW, Jardin R, et al. (2018) Size-strain separation in diffraction line profile analy-sis. J Appl Crystallogr 51: 831-843. [Crossref], [Google Scholar], [Indexed]
10. Evans JSO, Evans IR (2020) Structure analysis from powder diffraction data: Rietveld refinement in excel. J Chem Educ 98: 495-505. [Crossref], [Google Scholar]
11. Cheary RW, Coelho AA, Cline JP (2004) Fundamental parameters line profile fitting in laboratory diffractometers. J Res Natl Inst Stand Technol 109: 1-1. [Crossref], [Google Scholar], [Indexed]
12. Poppe R, Roth N, Neder RB, Palatinus L, Iversen BB, et al. (2023) Refining short-range order parameters from the three-dimensional diffuse scattering in single-crystal electron diffraction data. IUCrJ 11: 82-91 [Crossref], [Google Scholar], [Indexed]
13. Ozaki Y, Suzuki Y, Hawai T, Saito K, Onishi M, et al. (2020) Automated crystal structure analysis based on blackbox optimisation. npj Comput Mater 6. [Crossref], [Google Scholar]
14. Kawaguchi S, Kobayashi S, Yamada H, Ashitani H, Takemoto M, et al. (2024) High-throughput and high-resolution powder X-ray diffractometer consisting of six sets of 2D CdTe detectors with variable sample-to-detector distance and innovative automation system. J Synchrotron Radiat 31: 955-967. [Crossref], [Google Scholar], [Indexed]
15. Sperling Z (1995) Specimen displacement error in focusing systems. Powder Diffr 10: 278-281. [Crossref], [Google Scholar]
16. Cline JP, Mendenhall MH, Black D, Windover D, Henins A (2007) The optics and alignment of the divergent-beam laboratory X-ray powder diffractometer and its calibration using NIST standard reference materials. J Res Natl Inst Stand Technol 120: 173-222. [Crossref], [Google Scholar], [Indexed]
17. Hollarek D, Schopmans H, Östreicher J, Teufel J, Cao B, et al. (2025) opXRD: Open experimental powder X-ray diffraction database. [Crossref], [Google Scholar]
18. Wang C, Zhang R, Siu C, Ge M, Kisslinger K, et al. (2021) Chemomechanically stable ultrahigh-ni single-crystalline cathodes with improved oxygen retention and delayed phase degradations. Nano Lett 21: 9797-9804. [Crossref], [Google Scholar], [Indexed]